

Mitigated phase transition during first cycle of a Li-rich layered cathode studied by in operando synchrotron X-ray powder diffraction†

Received 00th January 20xx,
Accepted 00th January 20xx

DOI: 10.1039/x0xx00000x

www.rsc.org/

Bohang Song,^{a,†} Sarah J. Day,^b Tan Sui,^a Li Lu,^c Chiu C. Tang,^b Alexander M. Korsunsky^{a*}

In operando synchrotron X-ray powder diffraction (SXPD) studies were conducted to investigate the phase transition of Li-rich $\text{Li}(\text{Li}_{0.2}\text{Ni}_{0.13}\text{Mn}_{0.54}\text{Co}_{0.13})\text{O}_2$ and Cr-doped $\text{Li}(\text{Li}_{0.2}\text{Ni}_{0.13}\text{Mn}_{0.54}\text{Co}_{0.03}\text{Cr}_{0.10})\text{O}_2$ cathodes during the first charge/discharge cycle. Crystallographic (lattice parameters) and mechanical (domain size and microstrain) information was collected from SXPD full pattern refinement. It was found that Cr substitution at Co-site benefits in suppressing the activation of Li_2MnO_3 domains upon 1st charge, and thus mitigates the phase transition. As a consequence, Cr-doped layered cathode holds a better reversibility in terms of a full recovery of both lattice parameters and nano-domain size after a whole charge/discharge cycle. The effects of different cycling rates on the structural change were also discussed.

Introduction

Lithium-rich layered oxides have drawn extensive interest as cathode materials worldwide over the past decade in the field of lithium-ion batteries (LIBs). The nature of these materials leads to a high reversible capacity of over 250 mAh g^{-1} compared to 120 mAh g^{-1} of commercialized LiCoO_2 , acceptable thermal and structural stability, and low cost¹. However, one of the critical issues that must be addressed prior to full scale utilization as a cathode in LIBs is the so-called “voltage decay”, which is believed to be associated with the phase transformation inside individual particles that occurs in the very first cycle. It leads to voltage drop upon cycling, and thus the loss of the stored energy density of the whole battery system. The main phase in these Li-rich cathode materials is the rhomboheral LiMO_2 ($\text{M}=\text{Ni}$, Co , and/or Mn) that is accompanied by the monoclinic Li_2MnO_3 phase. The phase transformation mechanisms in these systems have been systematically studied in recent years^{2–5}. Armstrong et al.⁶ first demonstrated oxygen loss in association with Li removal in the compositional ratio of Li_2O , and the consequent structural reorganization upon the 1st charge/discharge cycling that is triggered by the transition metal (TM) migration from transition metal layer to a lithium layer vacancy. Gu et al.⁷

investigated the spinel formation in view of two different phases (rhombohedral $R\bar{3}m$ and monoclinic $C2/m$) by performing aberration-corrected scanning transmission electron microscopy (STEM) and electron energy loss spectroscopy (EELS). The results showed that the transformation in the $R\bar{3}m$ phase started from the surface and proceeded into the bulk of particles, and was accompanied by TM migration, and the nucleation and growth of spinel, whilst the transformation in the $C2/m$ phase was triggered by the oxygen loss and subsequent nano-nucleation of spinel-like nano-domains, as well as the formation of an amorphous phase in bulk. Gallagher et al.⁸ first demonstrated through a systematic electrochemical study the two steps of TM migration from a metastable tetragonal site to a localized and lower energy site to initiate spinel formation, which could be visualized from the hysteretic voltage decay.

A lot of effort has been dedicated to countering this spinel transformation to suppress the voltage decay which seems to be an inherent nature of Li-rich layered cathodes. Croy et al.⁹ proposed a “layered-rocksalt” composite, $x\text{Li}_2\text{MnO}_3 \cdot (1-x)\text{MO}$ (where M refers typically to Mn, Ni, and/or Co), to stabilize the local structure without compromising capacity, and achieved 245 mAh g^{-1} between 4.4 and 2.5 V at 15 mA g^{-1} after 60 cycles without obvious voltage decay. Recently, Sathiya et al.¹⁰ reported a series of novel $\text{Li}_2\text{Ru}_{1-y}\text{Sn}_y\text{O}_3$ cathodes with enhanced structural stability, which demonstrated a possible route to slow down the Td (tetrahedral position next to the LiM_2 layers) trapping by introducing large separator ions such as Sn. When Sn ratio increased from 25 to 50%, 50% decrease of voltage decay was reported in $\text{Li}_2\text{Ru}_{0.5}\text{Sn}_{0.5}\text{O}_3$. Zheng et al.¹¹ compared different synthesis methods and minimized the inhomogeneity of Ni distribution at the particle surface, which has proven to be beneficial for the suppression of voltage decay. Lee et al.¹² systematically investigated the effects of the

^a MBLEM, Department of Engineering Science, University of Oxford, Oxford OX1 3PJ, UK.

^b Diamond Light Source, Harwell Science and Innovation Campus, Didcot OX11 0DE, UK.

^c National University of Singapore, Department of Mechanical Engineering, Singapore.

† Current address: University of Texas at Austin, U.S.A.

† Electronic Supplementary Information (ESI) available: Morphology and electrochemical performance of P- and C-type cathodes, domain size and microstrain variations during high rate cycling. See DOI: 10.1039/x0xx00000x

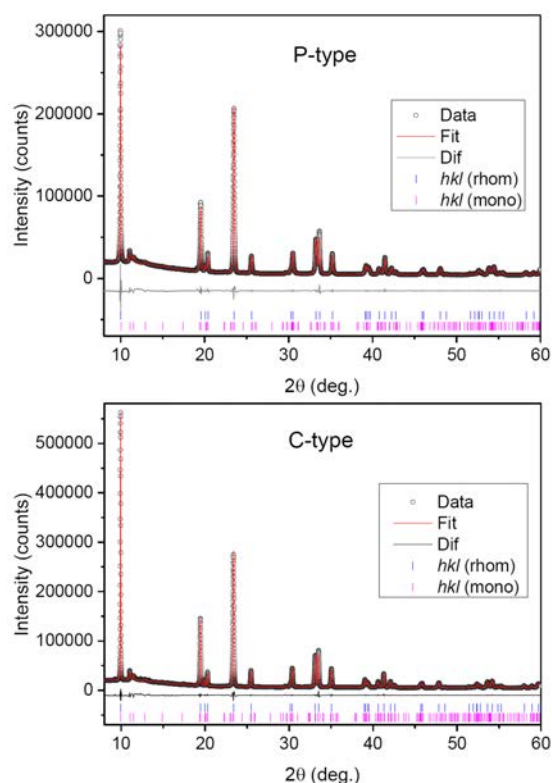


Fig. 1 SXPD patterns, fitted and difference data of P- and C-type powder materials and *hkl* reflections of the rhombohedral and monoclinic phases are presented as vertical lines below the difference curves.

4.5 V plateau length on the extent of voltage decay and found that the most suitable cathode composition of $\text{Li}_{1.15}\text{Mn}_{0.54}\text{Ni}_{0.23}\text{Co}_{0.08}\text{O}_2$ could be achieved without sacrificing much of the discharge capacity. Ates et al.¹³ also reported an effective strategy to mitigate this voltage decay by partial substitution of Li^+ ions with Na^+ , producing the $0.3\text{Li}_2\text{MnO}_3 \cdot 0.7\text{Li}_{0.97}\text{Na}_{0.03}\text{Mn}_{0.33}\text{Ni}_{0.33}\text{Co}_{0.33}\text{O}_2$ composition. According to the more recent work by Song et al.¹⁴, Cr-doping at the Co-site in Li-rich layered cathodes has benefits in mitigating the local phase transition by shortening the 4.5 V charging plateau, without sacrificing much reversible capacity due to $\text{Cr}^{3+/6+}$ redox compensation.

To acquire further insights into the structural stabilization mechanisms, pristine $\text{Li}(\text{Li}_{0.2}\text{Ni}_{0.13}\text{Mn}_{0.54}\text{Co}_{0.13})\text{O}_2$ (P-type) and Cr-doped $\text{Li}(\text{Li}_{0.2}\text{Ni}_{0.13}\text{Mn}_{0.54}\text{Co}_{0.03}\text{Cr}_{0.10})\text{O}_2$ (C-type) cathodes were studied while cycling at both slow and fast rates using *in operando* synchrotron X-ray powder diffraction (SXPD). It is well known that both the rhombohedral $R\bar{3}m$ - LiMO_2 and the monoclinic $C2/m$ - Li_2MnO_3 phases possess the α - NaFeO_2 -type of structure with a cubic-close-packed oxygen array, with all of

the octahedral sites occupied by Li and transition metals. This is the reason why their diffraction peaks are similar to each other, the only difference being due to the (020) and (110) peaks in the $C2/m$ phase. Whether this family of Li-rich layered cathodes are in the form of solid solution or composite structure, however, is still under debate. The most acceptable model is the nano-composite structure proposed by Thackeray et al.¹ and also reported by other groups¹⁵⁻¹⁶. In this model, there are Li_2MnO_3 -like and LiMO_2 -like nano-domains with short-range ordering in each domain due to the lack of Li-ions in the transition metal layer to sustain exact ratio of Li:TM at 1:2. In the current study, the diffraction data from powder samples was interpreted by two-phase refinement to allow quantitative analysis of the lattice structure and phase composition. For the *in operando* diffraction data during cycling, only the majority phase $R\bar{3}m$ was refined, similarly to most of the studies reported in the literature^{4, 17-19}. This is due to the fact that the majority of diffraction peaks of the $R\bar{3}m$ and $C2/m$ phases are coincident between the two phases, with only (020) and (110) peaks being belonging to the $C2/m$ phase only. Furthermore, upon cycling the intensity of the (020) and (110) $C2/m$ peaks gradually reduces due to the loss of the LiMn_6 superlattice that accompanies the removal of Li from structure.

Experimental

Preparation of battery materials and coin cells

Both pristine and Cr-doped cathode samples were synthesized by combining co-precipitation and solid-state reaction methods. The technical details of the process has been reported in our previous paper¹⁴. Scanning electron microscopy (SEM) images of each type of material are shown in Fig. S1 to demonstrate their morphologies and various particle sizes. To prepare the electrode slurry, active particles, carbon black (Super P), and Polyvinylidene Fluoride (PVDF) were homogeneously mixed together in a *n*-methyl-2-pyrrolidone (NMP) solution, in the weight ratio of 80 : 10 : 10. The slurry was then pasted onto an Al foil (25 μm thickness) before drying overnight to make it ready as an electrode. This electrode typically has the active material loading density of 5~6 mg/cm^2 .

Each synthesised material was loaded and tested using a normal battery coin cell. Fig. S2 demonstrates the suppression of voltage decay in the discharge curves from 1st to 60th cycle of Cr-doped cathode compared to the pristine material, whereas the specific capacities of these two are still comparable. For the synchrotron measurements, modified coin cells with X-ray windows at both beam entry and exit were used to assemble the lithium-ion batteries. For good X-ray transmission, thin Al foils (25 μm x 2) were used as X-ray windows. The P- and C-type battery cells were cycled between 4.9 and 1.5 V at low (50 $\text{mA}\cdot\text{g}^{-1}$) and high (250 $\text{mA}\cdot\text{g}^{-1}$) current density to compare the effects of electrochemical reactions.

In operando synchrotron X-ray diffraction experiments

Table 1 Lattice parameters of the as prepared P- and C-type samples.

Sample	$R\bar{3}m$		$C2/m$			β (°)
	a (Å)	b (Å)	a (Å)	b (Å)	c (Å)	
P-type	2.8512	14.225	4.9761	8.5252	4.9966	109.52
	1(1)	6(1)	(6)	(9)	(5)	5(9)
C-type	2.8634	14.279	4.9890	8.5541	5.0353	109.36
	7(1)	2(2)	(2)	(4)	(2)	1(2)

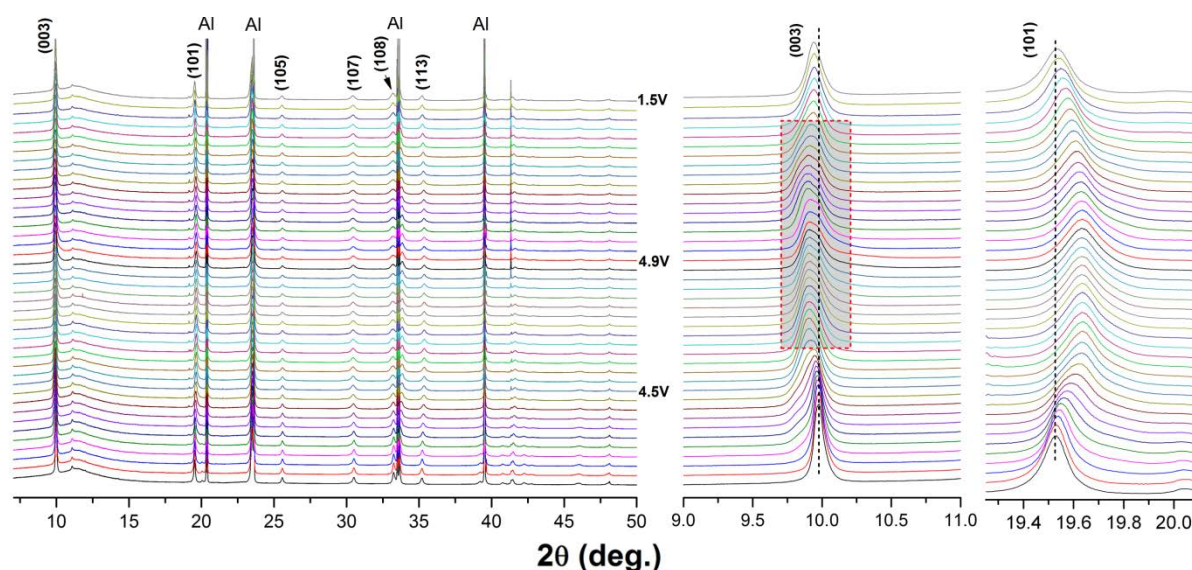


Fig. 2 Evolution of the X-ray diffraction patterns of P-type battery during 1st cycling at 50 mA g⁻¹. The enlarged parts (right) represent the evolution of the (003) and (101) peaks.

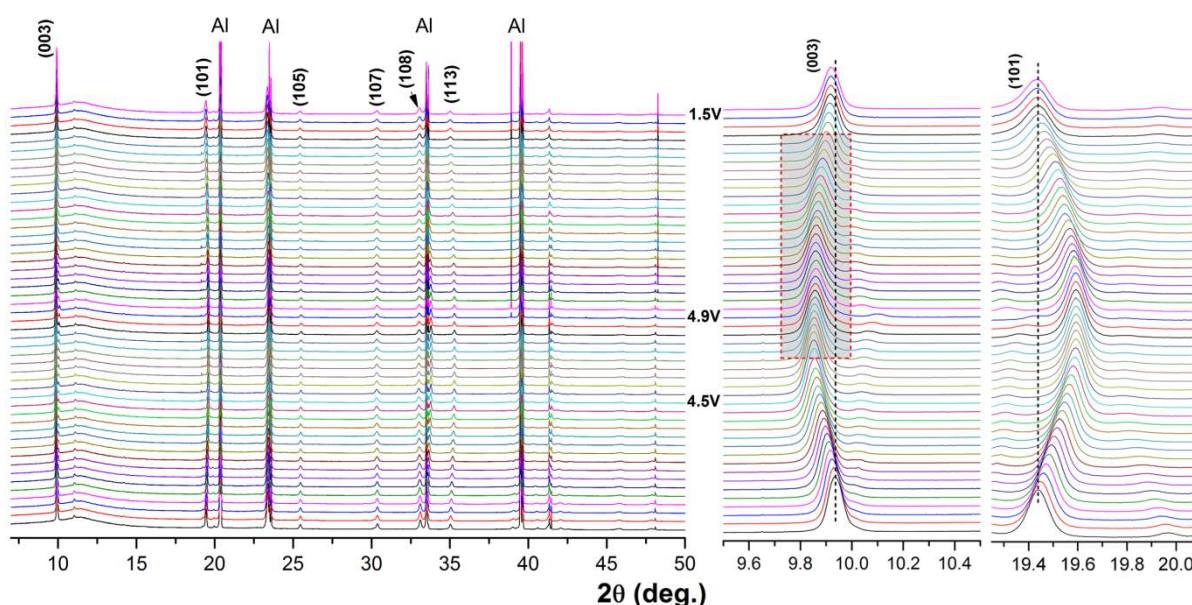


Fig. 3 Evolution of the X-ray diffraction patterns of C-type battery during 1st cycling at 50 mA g⁻¹. The enlarged parts (right) represent the evolution of (003) and (101) peaks.

During charge cycling, SXPD patterns were obtained using beamline I11 at Diamond Light Source (UK). The technical details for the instrument are given elsewhere²⁰⁻²¹. All measurements were performed in transmission mode using a monochromatic beam of $E=15$ keV. The wavelength was precisely calibrated using a high quality reference standard of NIST Si powder (SRM640c) to be $\lambda = 0.825985(10)$ Å. The high brightness incident beam and position-sensitive detector (PSD) permitted fast data collection at 20 s/pattern. A pattern was collected every 10 min during the 1st cycle of 50 mA g⁻¹ and 250 mA g⁻¹ charge/discharge rate of the two batteries. The data were analysed using TOPAS analysis software²². Several strong peaks were observed in the patterns using the battery cells, which correspond to Al foils (windows and electrode support) and have been excluded in the refinements. Although

full Rietveld refinement was not possible due to the overlaps between active materials and Al peaks, the unit cell parameter evolution could be monitored by whole pattern Pawley refinement. It provides an understanding of the unit cell distortion mechanism, as a and b parameters correspond to the slab dimensions, and c corresponds to the inter-slab distance. In addition, the broadening of diffraction peaks was de-convoluted from the instrumental contributions using Fundamental Parameters (FP) method²³ to extract the apparent particle, crystal or domain sizes, and micro-strain, together with the crystallographic details.

Results and discussion

Phase Characterisation Using High Resolution SXPD

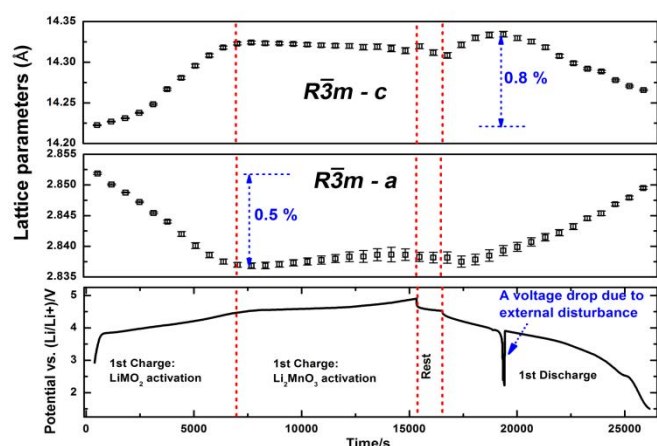


Fig. 4 Evolution of the lattice parameters of P-type during 1st cycling at 50 mA·g⁻¹.

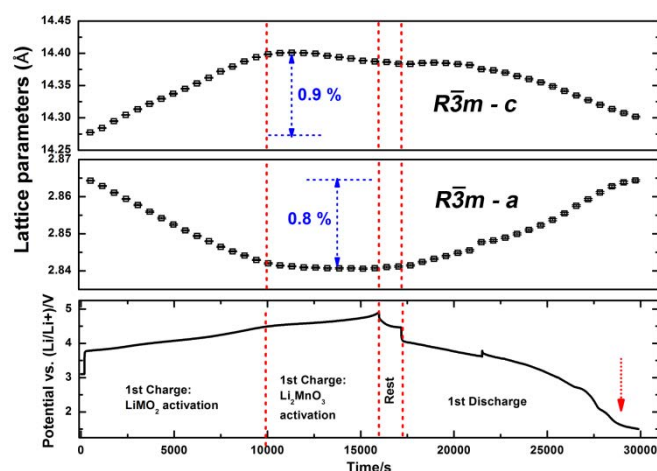


Fig. 5 Evolution of the lattice parameters of C-type during 1st cycling at 50 mA·g⁻¹.

As prepared samples were loaded in 0.5 mm diameter borosilicate capillaries and characterised with a 10 s SXP pattern each. The experimental data and fitted results are shown in Fig. 1. The main peaks for both active materials (P- and C-type) could be indexed as belonging to the $\text{LiNi}_{1/3}\text{Co}_{1/3}\text{Mn}_{1/3}\text{O}_2$ phase with $R\bar{3}m$ space group. In addition, the minor phase of Li_2MnO_3 ($C2/m$) was also present in both cathodes. As can be seen from Fig. 1, both patterns were fitted well with $R_{wp} = 4.27$ and 4.06% for the P- and C-type samples, respectively. The lattice parameters of the rhombohedral and monoclinic phases were obtained and are summarised in Table 1 for comparison. It should also be pointed out that the crystallographic results for the Li_2MnO_3 phase may not be reliable due its most intense peaks being superimposed with those from the R-3m structure. Only using a few weak peaks ($11 - 15^\circ 2\theta$ in Fig. 1) for the refinements could result in producing poor accuracy parameters. It is therefore difficult to crystallographically distinguish the minor $C2/m$ phase from the major R-3m phase, in particular using the operando data (next section) which included additional peaks from the Al-windows. We therefore only included the results from the refinements for the $\text{LiNi}_{1/3}\text{Co}_{1/3}\text{Mn}_{1/3}\text{O}_2$ as we with have no confidence with those obtained for the Li_2MnO_3 .

In operando analysis - Low Charge Rate

The evolution of *in situ* SXR patterns of P- and C-type during electrochemical cycling is shown in Figs. 2 and 3. The (*hkl*) peaks labelled in the figure correspond to the $R\bar{3}m$ space

group. As shown in the enlarged patterns, the evolution of the (003) peak shows a difference between the pristine and Cr-doped cathodes. For the P-type battery, this peak shifts slightly toward the lower angle and exhibits significant broadening, starting from early stage of charging to the end of discharge. Such broadening of peaks could be ascribed to two reasons, the first of which is the extension of disordered phase and stacking faults during (de)intercalation of Li. The second is the nucleation and growth of a new phase, as suggested by the splitting of the (003) peak when charging to around 4.5 V, and emphasized by the grey rectangle in the enlarged patterns of Fig. 2. If the latter mechanism dominates, then this observation is quite consistent with previous reports on the lattice rearrangement from layered to spinel-like ordering, which also involves TM migration from the TM layer to the Li layer⁶⁻⁷. Interestingly, in the Cr doped sample, the (003) peak shifts significantly to a lower angle but with less broadening of peaks during charge/discharge, as emphasized by the grey rectangle in enlarged patterns of Fig. 3, indicating relatively small structural change in the local lattice as a result of (de)intercalation of Li. This observation implies enhanced stability, and better reversibility of Cr-doped material. The better reversibility could also be identified in terms of the evolution of (003) and (101) peaks which are associated with the *a* and *c* lattice parameters, respectively. They are seen to evolve in opposite directions during cycling: the (101) peak shifts from higher angle back to its original position in the case of C-type during discharge, whereas it only partially shifts back under the same conditions for the P-type sample. It is speculated that Cr-doping stabilizes and/or tunes the electronic configurations of the $C2/m$ phase, with only partial activation of it as a consequence. Meanwhile, the deintercalation of Li accompanied with Cr^{3+} oxidation to Cr^{6+} may suppress the O^{2-} oxidation reaction to O^- ²⁴⁻²⁵. This finding may provide an explanation of why Cr-doping has benefits in mitigating the voltage decay in subsequent cycles, as reported by Song et al.¹⁴. Note that the $C2/m$ phase activation with a removal of Li_2O is the main reason for the phase transition and voltage decay. Such mechanism change as mentioned above of Li removal from the $C2/m$ phase is also the reason why Cr-doping of the cathode shortens the length of the 4.5 V plateau, as will be shown in Figs. 4 and 5. It is also worth pointing out that the activation depths of both P- and C-type electrodes must be comparable and have similar effects on reversibility. In fact, the C-type delivers more discharge capacity, meaning that more active particles take part in the electrochemical reaction than P-type, therefore leading to better reversibility. Fig. 4 shows the evolution of the *a* and *c* lattice parameters of P-type cathodes during the 1st cycle, with charging and discharging stages labelled. During the 1st charge activation of $R\bar{3}m$ phase from open circuit voltage (OCV) to 4.5 V, the *a* parameter gradually decreases, which is commonly related to the oxidation of transition metals in the TM layer resulting in reduced atomic radii. Meanwhile, the *c* parameter gradually increases, which is regarded to be the result of Li removal from metallic layer, leading to a decrease of the screening effect between the oxygen layers. At the second stage of the 1st

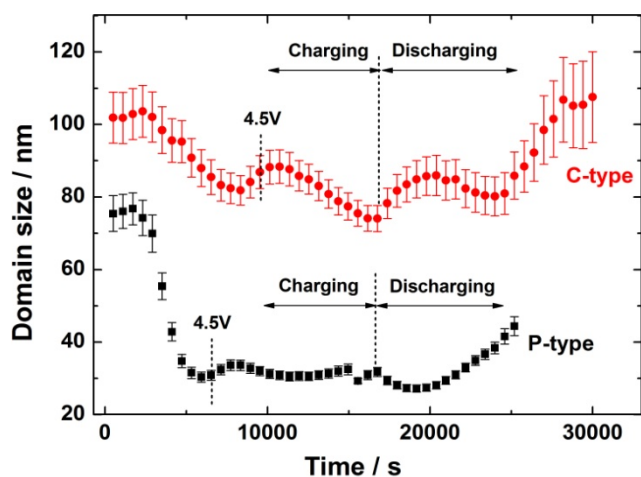


Fig. 6 Domain size variations during first charge/discharge cycle of both pristine and Cr-doped cathodes at 50 mA·g⁻¹.

charging, i.e. the activation of the C2/m phase, both a and c lattice parameters of the $R\bar{3}m$ phase remain stable showing no obvious variation, although Li is further extracted from the local structure. This behaviour is commonly regarded as a biphasic process, which is consistent with the plateau observation from the charging curve²⁶. During the 1st discharging stage, both a and c parameters of the $R\bar{3}m$ phase tend to recover back to their original value, meaning a partially-reversible process of Li reinsertion. In contrast, the C-type cathode shown in Fig. 5, exhibits similar tendencies for the a and c parameters of the $R\bar{3}m$ phase, but better reversibility in terms of the close value of lattice parameters between fresh and the 1st discharged state. Besides, comparing the variation ratios of lattice parameters upon the 1st cycle for P- and C-type cathodes also indicates a similar value of their maximum relative change due to (de)intercalation of Li from $R\bar{3}m$ phase.

The refined particle sizes are between 30 – 100 nm, as shown in Fig. 6. This is considerably smaller than the particles seen in the SEM images (Fig. S1). As X-rays only “see” diffraction entities, each particle must therefore contain smaller coherently scattering domains. We therefore refer to the size parameters deduced from diffraction (and hereafter) as crystallite or domain sizes. Fig. 6 compares the domain size evolution during the 1st charge/discharge cycle between P- and C-type cathodes based on the results of FP-refinements. The domain size of pristine Li-rich material dramatically decreases from 75 to 30 nm that corresponds to the OCV and 4.5 V charging point. It implies a consistent change of domain size with the volume change of $R\bar{3}m$ phase as a result of deintercalation of Li. However, such decrease stops between 4.5 and the cut-off charging point of 4.9 V (the plateau region as indicated in Fig. 4). Note that both a and c lattice parameters of $R\bar{3}m$ phase exhibit almost no change in this voltage range according to Fig. 4 (1st Charge: Li₂MnO₃

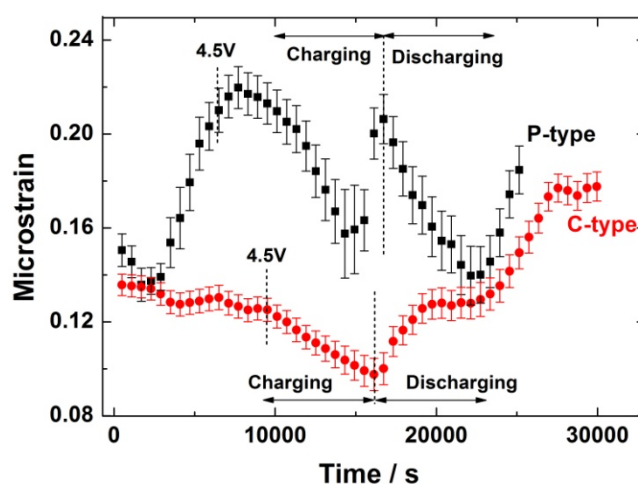


Fig. 7 Microstrain variations during first charge/discharge cycle of both pristine and Cr-doped cathodes at 50 mA·g⁻¹.

activation), suggesting again the domain size change is consistent with the volume change during activation. Upon discharge, the crystallites keep increasing from 30 to 44 nm due to the reinsertion of Li into lattice. On the other hand, after Cr doping, although the domain size of C-type reduces similarly from 100 to 80 nm due to Li removal from $R\bar{3}m$ phase, it continuously reduces further from 80 to 74 nm as a result of Li₂MnO₃ activation. This observation suggests again that the Li₂MnO₃ activation in C-type cathode may possess a different reaction mechanism compared to P-type, which is very likely to be related with the Cr^{3+/6+} redox reaction. On discharge, the domain size keeps increasing from 74 to 107 nm that is even bigger than the initial value.

Thus, it is important to point out two main findings:

- (1) The decremental ratio of crystal size for C-type upon charging (27 %) is significantly less than the corresponding value of P-type (59 %).
- (2) The domain size of C-type material is reversibly recovered upon the whole charge/discharge process, whereas P-type fails to recover fully. Both of these findings suggest a better reversibility of Cr-doped Li-rich cathode compared to the pristine material as Li host structure.

Fig. 7 shows the microstrain variation of both P- and C-type cathodes upon the 1st charge/discharge cycle. Such microstrain in domains could be ascribed to the high vacancy concentration during high temperature sintering, Li vacancy generation during (de)intercalation, lattice disorder, phase transition, etc. It is apparent that the microstrain evolution of C-type is coherent and reversible during the charge and discharge processes, whereas it is much more complex in the case of P-type. In addition, the highest value is 0.17 for the C-type material, which is significantly less than 0.22 for the P-type.

In operando analysis - High Charge Rate

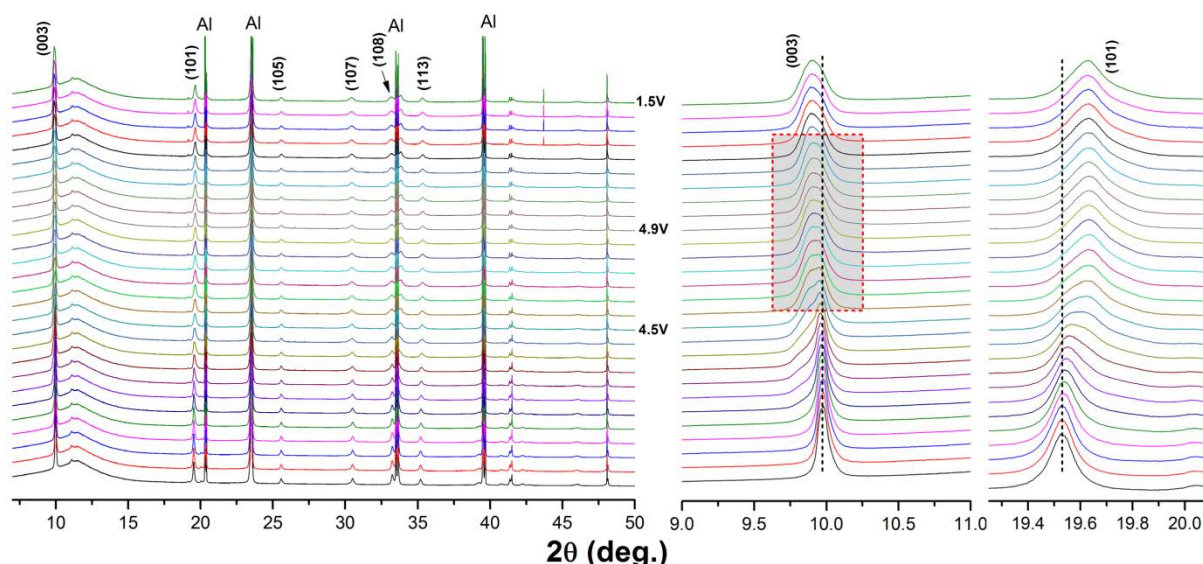


Fig. 8 Evolution of the SXPD patterns of P-type during 1st cycling at 250 mA·g⁻¹. The enlarged parts represent the evolution of (003) and (101) peaks.

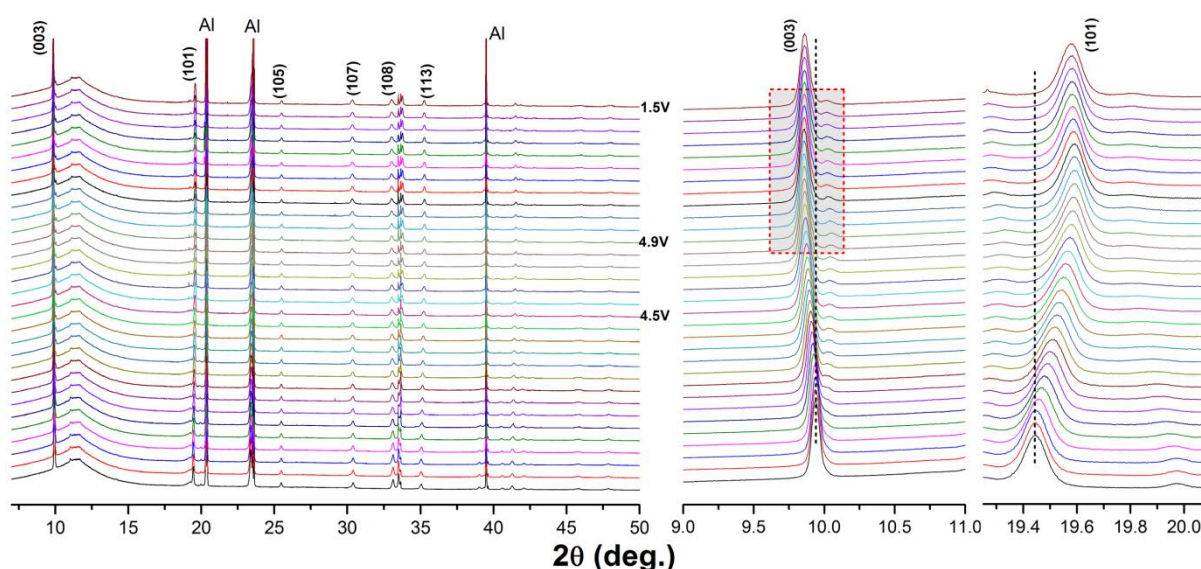


Fig. 9 Evolution of the SXPD patterns of C-type during 1st cycling at 250 mA·g⁻¹. The enlarged parts represent the evolution of (003) and (101) peaks.

To investigate the mechanism changes of the crystal structure due to high rate cycling, the current density was increased to 250 mA·g⁻¹ and the in operando SXPD experiment was carried out for the two types of battery. The diffraction results for the P-type cathode are presented in Fig. 8. The (003) peak shifts to lower angle whilst the (101) peak shifts to higher angle upon 1st charging process. However, it is apparent that they are not able to shift back upon 1st discharge, indicating less reversibility of Li reinsertion at such a high current density. As in the low rate cycling, the splitting of the (003) peak was observed at about 4.5 V but was more pronounced, as highlighted by the grey region in the figure, suggesting an activation of the Li₂MnO₃ component and thus phase transition even at such a high rate. In contrast, the C-type cathode shows significant difference upon the 1st cycle (Fig. 9). Specifically, the peak broadening of the (003) and (101) reflections is not obvious, with peaks remaining sharp and

devoid of splitting when charging to voltages higher than 4.5 V. In fact, these observations agree well with the charge curves shown in Figs. 10 and 11, since the 4.5 V charging plateau disappears in the case of C-type but still shows up for the P-type. The reason might be that the reaction kinetics of removing Li from Li₂MnO₃ component in the C-type is even worse than the case of P-type because of Cr presence, or it could be due to the sluggish three-electron reaction of the Cr^{3+/6+} redox (Fig. S3).

Fig. 10 shows the variations of lattice parameters *a* and *c* for the *R* $\bar{3}m$ component of the P-type material when cycled at the high rate. During the first step of charging from OCV to 4.5 V, both *a* and *c* parameters of the *R* $\bar{3}m$ phase change in accordance with the results at the low rate, indicating successful removal of Li from this phase. Upon discharging, both *a* and *c* lattice parameters only change slightly, which can be reasonably ascribed to the fast discharging rate that results

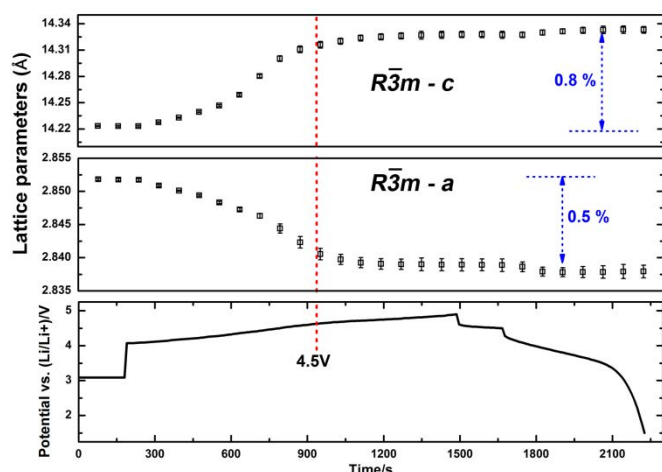


Fig. 10 Evolution of the cell parameters of P-type during 1st cycling at 250 mA·g⁻¹.

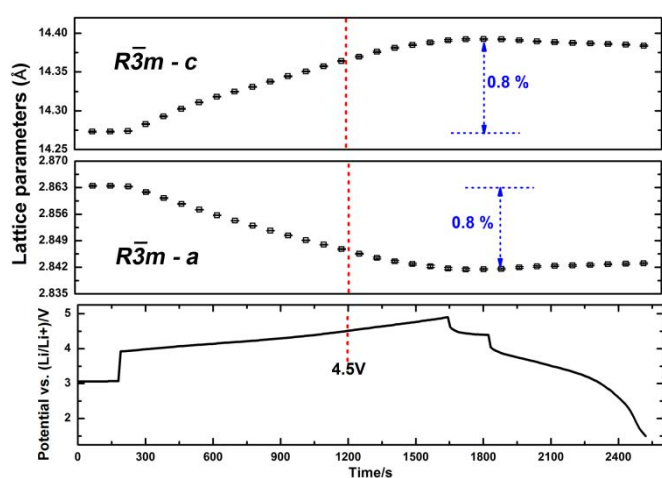


Fig. 11 Evolution of the cell parameters of C-type during 1st cycling at 250 mA·g⁻¹.

in Li aggregation at particle surface without sufficient time for diffusion into the bulk lattice to take place. Such poor reversibility is quite consistent with the observation of the shortened discharge curve.

Fig. 11 shows the variation of the unit cell parameters a and c of the C-type material when cycled at a high rate of 250 mA·g⁻¹. It is important to note that following the initial change of both a and c parameters of the $R\bar{3}m$ phase at the end of the 4.5 V plateau, they continue to vary up to the cut-off voltage, suggesting a further removal of Li from the $R\bar{3}m$ phase, that is different from P-type. The reason might be that the Cr^{3+/6+} redox reaction continues to contribute electrons and thus varies the lattice constants in this voltage range even at such high current density. Similarly, reintercalation of Li upon fast discharge leads to no obvious change of both lattice parameters, implying a poor reversibility of C-type cathode at a high rate of cycling. Fig. S4 shows the domain size evolution of both samples at the high rate. Initially, in both the P- and C-type, the domain dramatically reduces from 66 to 30 nm and 103 to 76 nm, respectively, before reaching 4.5 V, which is in accordance with the trends obtained at the low rate. However, neither of them is able to recover during discharge, indicating poor reversibility of both samples in terms of domain size. Fig.

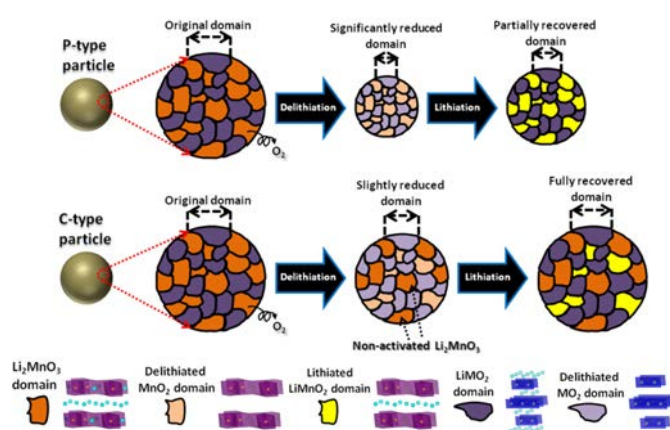


Fig. 12 A schematic illustration of delithiation/lithiation mechanism based on nano-domain structures during 1st cycle at a low rate of cycling.

S5 shows the microstrain variation upon fast charge/discharge. Although both P- and C-type cathodes present increased microstrain due to deintercalation of Li, their values are relatively steady during the reinsertion of Li. It suggests that in both cases the amount of reinserted Li into the crystal lattice is limited because of the limited diffusion time. It could be concluded that both materials are of poor rate capability based on the above observations.

Discussion: the delithiation/lithiation mechanism

To represent the main findings more clearly, a schematic illustration is shown in Fig. 12. The initial charging process during the 1st cycle of the P-type [pristine Li(Li_{0.2}Mn_{0.54}Ni_{0.13}Co_{0.13})O₂] cathode significantly reduces the domain size due to Li removal. Whilst similar behaviour is observed in the case of C-type [Cr-doped, Li(Li_{0.2}Ni_{0.13}Mn_{0.54}Co_{0.03}Cr_{0.10})O₂] cathode, it progresses to a lesser extent compared to the P-type. Full recovery of domain size as a result of relithiation upon 1st discharge is revealed for the Cr-doped cathode, indicating a better reversibility as Li host after doping, compared to the partial recovery of the pristine cathode. Meanwhile, it seems that although the $R\bar{3}m$ -LiMO₂ phase could fully participate in the delithiation reaction in both cathodes, only a partial amount of the $C2/m$ -Li₂MnO₃ phase is activated in case of Cr-doped one, leading to a considerable degree of coexistence between the original Li₂MnO₃ and the transformed-LiMnO₂ phases in the local lattice after a full cycle. This finding provides a possible explanation for the mitigated phase transition due to Cr doping, which confers further benefit during the following cycles.

Conclusions

We have produced pristine Li(Li_{0.2}Ni_{0.13}Mn_{0.54}Co_{0.13})O₂ and Cr-doped Li(Li_{0.2}Mn_{0.54}Ni_{0.13}Co_{0.03}Cr_{0.10})O₂ Li-ion battery samples for *in operando* synchrotron X-ray diffraction studies. These Li-rich layered compounds are good cathode materials, as confirmed by the charge/discharge cycling data from loaded coin cells. Most importantly, crystallographic and mechanical

(domain size and microstrain) information was obtained from XSPD full pattern refinements. The results from the *in operando* experiment at the low charge rate (50 mA g^{-1}) show the remarkable finding that Cr substitution in the Li-rich layered system has benefits in stabilizing the local structure by suppressing the amount of Li_2MnO_3 activation, and thus mitigates the inevitable phase transformation during the 1st cycle. Additionally, the full recovery of lattice domains upon Li (de)intercalation demonstrates its structural reversibility as Li host. Nevertheless, the loss of capacity as a result of less Li_2MnO_3 activation could be compensated by initiating the $\text{Cr}^{3+}/\text{Cr}^{6+}$ redox reaction, which makes this doped material very promising as a high energy density cathode. Furthermore, the results from the high rate (250 mA g^{-1}) cycling experiment reveal a poor rate capability for both pristine and Cr-doped cathodes. More studies on the structural evolution upon extended cycles are in progress for further assessment of the performance of this type of cathode material.

Acknowledgements

AMK acknowledges funding received for the Multi-Beam Laboratory for Engineering Microscopy (MBLEM) at Oxford through EU FP7 project iSTRESS (604646), and the provision of facilities at the Research Complex at Harwell (RCaH) for the Centre for In situ Processing Studies (CIPS).

Notes and references

1. M. M. Thackeray, S. H. Kang, C. S. Johnson, J. T. Vaughey, R. Benedek and S. A. Hackney, *J. Mater. Chem.*, 2007, **17**, 3112-3125.
2. J. M. Zheng, M. Gu, J. Xiao, P. J. Zuo, C. M. Wang and J. G. Zhang, *Nano Lett.*, 2013, **13**, 3824-3830.
3. M. Gu, A. Genc, I. Belharouak, D. P. Wang, K. Amine, S. Thevuthasan, D. R. Baer, J. G. Zhang, N. D. Browning, J. Liu and C. M. Wang, *Chem. Mat.*, 2013, **25**, 2319-2326.
4. D. Mohanty, S. Kalnaus, R. A. Meisner, K. J. Rhodes, J. L. Li, E. A. Payzant, D. L. Wood and C. Daniel, *J. Power Sources*, 2013, **229**, 239-248.
5. N. Yabuuchi, K. Yoshii, S. T. Myung, I. Nakai and S. Komaba, *J. Am. Chem. Soc.*, 2011, **133**, 4404-4419.
6. A. R. Armstrong, M. Holzapfel, P. Novak, C. S. Johnson, S. H. Kang, M. M. Thackeray and P. G. Bruce, *J. Am. Chem. Soc.*, 2006, **128**, 8694-8698.
7. M. Gu, I. Belharouak, J. M. Zheng, H. M. Wu, J. Xiao, A. Genc, K. Amine, S. Thevuthasan, D. R. Baer, J. G. Zhang, N. D. Browning, J. Liu and C. M. Wang, *ACS Nano*, 2013, **7**, 760-767.
8. K. G. Gallagher, J. R. Croy, M. Balasubramanian, M. Bettge, D. P. Abraham, A. K. Burrell and M. M. Thackeray, *Electrochem. Commun.*, 2013, **33**, 96-98.
9. J. R. Croy, D. Kim, M. Balasubramanian, K. Gallagher, S. H. Kang and M. M. Thackeray, *J. Electrochem. Soc.*, 2012, **159**, A781-A790.
10. M. Sathiya, A. M. Abakumov, D. Foix, G. Rousse, K. Ramesha, M. Saubanere, M. L. Doublet, H. Vezin, C. P. Laisa, A. S. Prakash, D. Gonbeau, G. VanTendeloo and J. M. Tarascon, *Nat. Mater.*, 2015, **14**, 230-238.
11. J. M. Zheng, M. Gu, A. Genc, J. Xiao, P. H. Xu, X. L. Chen, Z. H. Zhu, W. B. Zhao, L. Pullan, C. M. Wang and J. G. Zhang, *Nano Lett.*, 2014, **14**, 2628-2635.
12. E. S. Lee and A. Manthiram, *J. Mater. Chem. A*, 2014, **2**, 3932-3939.
13. M. N. Ates, Q. Y. Jia, A. Shah, A. Busnaina, S. Mukerjee and K. M. Abraham, *J. Electrochem. Soc.*, 2014, **161**, A290-A301.
14. B. H. Song, C. F. Zhou, H. L. Wang, H. W. Liu, Z. W. Liu, M. O. Lai and L. Lu, *J. Electrochem. Soc.*, 2014, **161**, A1723-A1730.
15. S. H. Yu, T. Yoon, J. Mun, S. Park, Y. S. Kang, J. H. Park, S. M. Oh and Y. E. Sung, *J. Mater. Chem. A*, 2013, **1**, 2833-2839.
16. J. Bareno, M. Balasubramanian, S. H. Kang, J. G. Wen, C. H. Lei, S. V. Pol, I. Petrov and D. P. Abraham, *Chem. Mat.*, 2011, **23**, 2039-2050.
17. C. H. Shen, Q. Wang, F. Fu, L. Huang, Z. Lin, S. Y. Shen, H. Su, X. M. Zheng, B. B. Xu, J. T. Li and S. G. Sun, *ACS Appl. Mater. Interfaces*, 2014, **6**, 5516-5524.
18. X. Q. Yu, Y. C. Lyu, L. Gu, H. M. Wu, S. M. Bak, Y. N. Zhou, K. Amine, S. N. Ehrlich, H. Li, K. W. Nam and X. Q. Yang, *Adv. Energy Mater.*, 2014, **4**.
19. L. Simonin, J. F. Colin, V. Ranieri, E. Canevet, J. F. Martin, C. Bourbon, C. Baetz, P. Strobel, L. Daniel and S. Patoux, *J. Mater. Chem.*, 2012, **22**, 11316-11322.
20. S. P. Thompson, J. E. Parker, J. Marchal, J. Potter, A. Birt, F. Yuan, R. D. Fearn, A. R. Lennie, S. R. Street and C. C. Tang, *J. Synchrotr. Radiat.*, 2011, **18**, 637-648.
21. S. P. Thompson, J. E. Parker, J. Potter, T. P. Hill, A. Birt, T. M. Cobb, F. Yuan and C. C. Tang, *Rev. Sci. Instrum.*, 2009, **80**.
22. *DIFFRAC PLUS, Version 4.2, Bruker AXS GmbH, Karlsruhe, Germany*, 2009.
23. R. W. Cheary and A. Coelho, *J. Appl. Crystallogr.*, 1992, **25**, 109-121.
24. M. Sathiya, K. Ramesha, G. Rousse, D. Foix, D. Gonbeau, A. S. Prakash, M. L. Doublet, K. Hemalatha and J. M. Tarascon, *Chem. Mat.*, 2013, **25**, 1121-1131.
25. N. Yabuuchi, K. Yamamoto, K. Yoshii, I. Nakai, T. Nishizawa, A. Omaru, T. Toyooka and S. Komaba, *J. Electrochem. Soc.*, 2013, **160**, A39-A45.
26. A. K. Padhi, K. S. Nanjundaswamy and J. B. Goodenough, *J. Electrochem. Soc.*, 1997, **144**, 1188-1194.

Graphical Table of Contents

This paper reports a *in operando* synchrotron X-ray powder diffraction (SXPDP) study on Li-rich $\text{Li}(\text{Li}_{0.2}\text{Ni}_{0.13}\text{Mn}_{0.54}\text{Co}_{0.13})\text{O}_2$ and Cr-doped $\text{Li}(\text{Li}_{0.2}\text{Ni}_{0.13}\text{Mn}_{0.54}\text{Co}_{0.03}\text{Cr}_{0.10})\text{O}_2$ cathodes during the first charge/discharge cycle. It was found that Cr-doping benefits in stabilizing local structure by suppressing the activation of Li_2MnO_3 domains.

Keywords: *in operando* synchrotron X-ray powder diffraction, lithium-rich layered cathodes, phase transition, lithium-ion batteries

Title: Mitigated phase transition during first cycle of a Li-rich layered cathode studied by *in operando* synchrotron X-ray powder diffraction

